Vapor-Phase Atomic-Controllable Growth of Amorphous Li_2S for High-Performance Lithium–Sulfur Batteries

Xiangbo Meng,[†] David J. Comstock,[†] Timothy T. Fister,[‡] and Jeffrey W. Elam[*,†]

[†]Energy Systems Division and [‡]Chemical Sciences and Engineering Division, Argonne National Laboratory, 9700 South Cass Avenue, Argonne, Illinois 60439, United States

ABSTRACT Lithium–sulfur (Li–S) batteries hold great promise to meet the formidable energy storage requirements of future electrical vehicles but are prohibited from practical implementation by their severe capacity fading and the risks imposed by Li metal anodes. Nanoscale Li_2S offers the possibility to overcome these challenges, but no synthetic technique exists for fine-tailoring Li_2S at the nanoscale. Herein we report a vapor-phase atomic layer deposition (ALD) method for the atomic-scale-controllable synthesis of Li_2S. Besides a comprehensive investigation of the ALD Li_2S growth mechanism, we further describe the high performance of the resulting amorphous Li_2S nanofilms as cathodes in Li–S batteries, achieving a stable capacity of ~800 mA·h/g, nearly 100% Coulombic efficiency, and excellent rate capability. Nanoscale Li_2S holds great potential for both bulk-type and thin-film high-energy Li–S batteries.

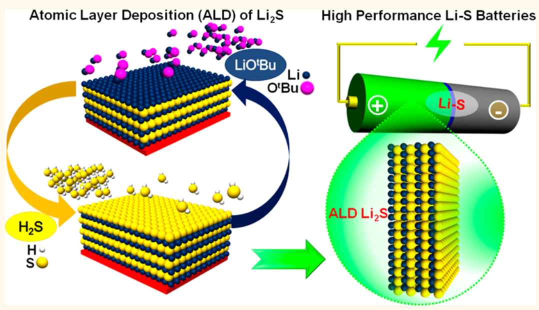

KEYWORDS: atomic layer deposition · lithium–sulfur battery · nanoscale Li_2S films

Electrical energy storage systems are essential for the wide-scale implementation of sustainable clean energy alternatives to fossil fuels such as solar power and wind.[1] Although incremental improvements have allowed lithium-ion batteries (LIBs) to dominate the portable consumer electronics market,[2,3] their low theoretical energy density (360 Wh/kg for $LiCoO_2$/graphite) is insufficient for powering electrical vehicles and smart grids.[2,3] In contrast, the very high theoretical energy density of lithium–sulfur (Li–S) batteries (2600 Wh/kg) makes them an attractive alternative.[4−6] However, daunting technical challenges must be overcome before Li–S batteries can be commercialized,[4,7,8] including poor electrode rechargeability and limited rate capability due to the electronically and ionically insulating nature of S and Li_2S. Moreover, the lithium anode presents the risk of dendrite formation during cycling that can cause catastrophic failure.[4] A viable solution to these problems is to substitute the S cathode with a Li_2S/carbon nanocomposite, wherein the carbon provides high conductivity and Li-ions incorporated in the cathode permit replacing the hazardous metallic Li anode with a benign alternative such as Si or Sn.[4]

Previously, ball milling[9−16] and other techniques[17−19] have been used to mix carbon[9−14,17,19,20] and metals[15,16,18] with Li_2S to improve conductivity. Furthermore, solid-state electrolytes[12−16,21] have been explored for improved safety and ionic conductivity in Li–S batteries. These studies unanimously demonstrated that dimensional reduction of the Li_2S (from micro- to nanosized) is crucial to achieve high capacity retention, cycling stability, and rate[9−16,19] because nanosized Li_2S has an ionic conductivity higher than that of the bulk[21] and is less susceptible to disintegration from repeated cycling.[14,22] To date, no synthetic approach has emerged with the precision required for nanoscale dimensional control, which is paramount to producing the Li_2S composites required for successful Li–S batteries. In addition to its role in Li–S batteries, Li_2S is critical in solid electrolytes which are regarded as an ultimate solution for mitigating the battery safety issues[23−25] imposed by flammable, organic liquid electrolytes. Sulfide-based materials exhibit the highest ionic conductivity of any solid electrolyte,[26] rivaling that of liquid electrolytes.

* Address correspondence to jelam@anl.gov.

Received for review August 29, 2014 and accepted October 13, 2014.

Published online October 13, 2014
10.1021/nn505480w

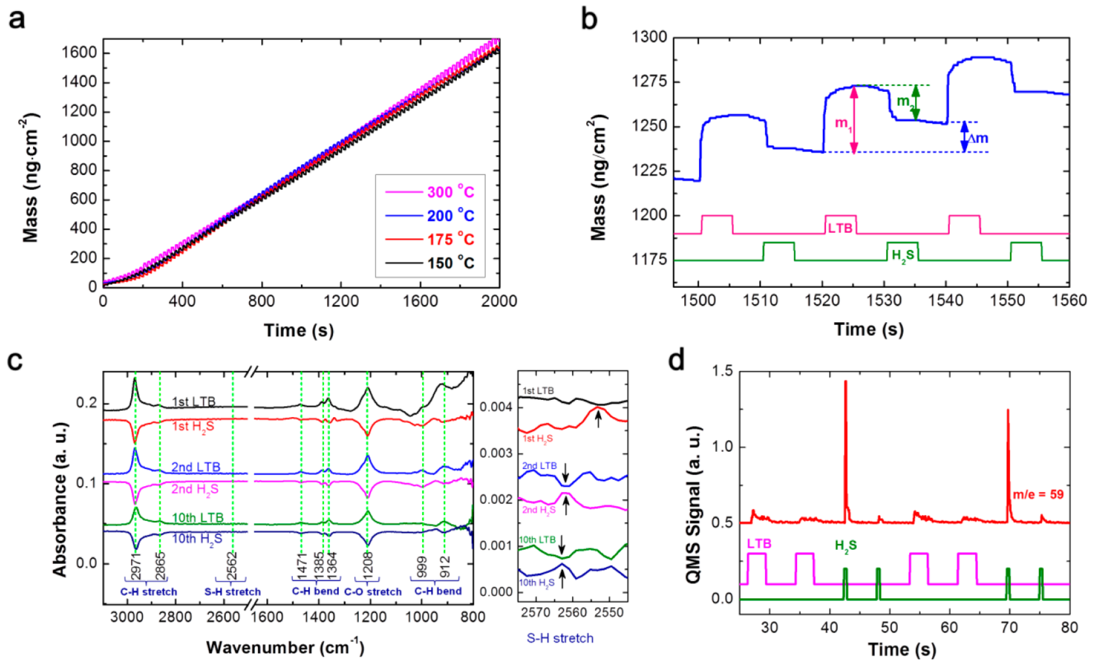

Figure 1. Investigation of surface chemistry for Li_2S ALD. (a,b) *In situ* QCM measurements of Li_2S ALD at 150, 175, 200, and 300 °C using the timing sequence 5−5−5−5 s: (a) mass of Li_2S film *versus* time during 100 ALD cycles and (b) enlarged view of three consecutive Li_2S ALD cycles performed at 150 °C in the regime of constant growth per cycle (precursor pulsing is indicated by lower traces, and m_1, m_2, and Δm are described in the text). (c) *In situ* FTIR difference spectra recorded after individual LTB and H_2S exposures during the first, second, and 10th ALD cycles on an ALD Al_2O_3 surface at 225 °C; right-hand spectra show expanded views of the S−H stretching region. (d) *In situ* QMS measurements during two consecutive Li_2S ALD cycles at 225 °C, where the LTB and H_2S precursors are each dosed twice (dosing indicated by lower traces) to reveal possible background signals.

Herein we introduce the atomically precise synthesis of nano-Li_2S using a vapor-phase atomic layer deposition (ALD) *via* alternating exposures to lithium *tert*-butoxide (LTB, $LiOC(CH_3)_3$) and hydrogen sulfide (H_2S). ALD relies on surface-controlled chemistry to accomplish layer-by-layer growth with sub-nanometer thickness control[27] and has evolved into a versatile technique for nanostructured material synthesis.[28,29] We employed a suite of *in situ* measurements and *ex situ* characterization methods to establish the conditions for self-limiting growth, elucidate the Li_2S ALD mechanism, and characterize the materials. Next, we fabricated both pure Li_2S nanofilms and nanoscale composites of carbon-supported Li_2S using this ALD route and integrated them into thin-film and bulk-type Li−S batteries exhibiting high storage capacity and excellent cyclability.

RESULTS AND DISCUSSION

***In Situ* Investigation of Atomic-Scale Growth Mechanism of ALD Li_2S.** A thorough understanding of the underlying surface chemistry can be crucial for implementing ALD processes, particularly when infiltrating porous materials to produce advanced electrodes or for scaling to larger area substrates.[30] To this end, *in situ* quartz crystal microbalance (QCM), quadrupole mass spectrometry (QMS), and Fourier transform infrared spectroscopy (FTIR) measurements were combined to elucidate the growth mechanism and to evaluate the range of conditions suitable for nano-Li_2S ALD. Figure 1a shows the time-resolved mass changes observed by *in situ* QCM during 100 alternating exposures to LTB and 1% H_2S for Li_2S ALD performed at 150, 175, 200, and 300 °C on an ALD Al_2O_3 starting surface. It is evident that the alternating LTB/H_2S exposures deposit material at a relatively constant rate independent of substrate temperature. The substrate-inhibited growth observed during the first 20 ALD cycles on the Al_2O_3 starting surface might result from surface poisoning by residual *tert*-butoxy ligands as will be discussed below for the FTIR measurements. Figure 1b shows an enlarged view of three consecutive Li_2S ALD cycles highlighting the mass changes resulting from individual LTB and H_2S exposures. The LTB exposures cause a mass increase $m_1 = \sim 36\ \mathrm{ng\cdot cm^{-2}\cdot cycle^{-1}}$, while the H_2S exposures decrease the mass by $m_2 = \sim 19\ \mathrm{ng\cdot cm^{-2}\cdot cycle^{-1}}$ to yield a net mass change $\Delta m = \sim 17\ \mathrm{ng\cdot cm^{-2}\cdot cycle^{-1}}$. These mass changes can be used to establish the mechanism for Li_2S ALD assuming the following reactions:

$$|-(\mathrm{SH})_x + \mathrm{LiO}^t\mathrm{Bu(g)} \rightarrow |-\mathrm{S}_x - \mathrm{Li(O}^t\mathrm{Bu)}_{(1-x)} + x\mathrm{HO}^t\mathrm{Bu(g)} \quad (1a)$$

$$|-\mathrm{S}_x - \mathrm{Li(O}^t\mathrm{Bu)}_{(1-x)} + 0.5\mathrm{H_2S(g)} \rightarrow |-(\mathrm{LiS}_{0.5})-(\mathrm{SH})_x + (1-x)\mathrm{HO}^t\mathrm{Bu(g)} \quad (1b)$$

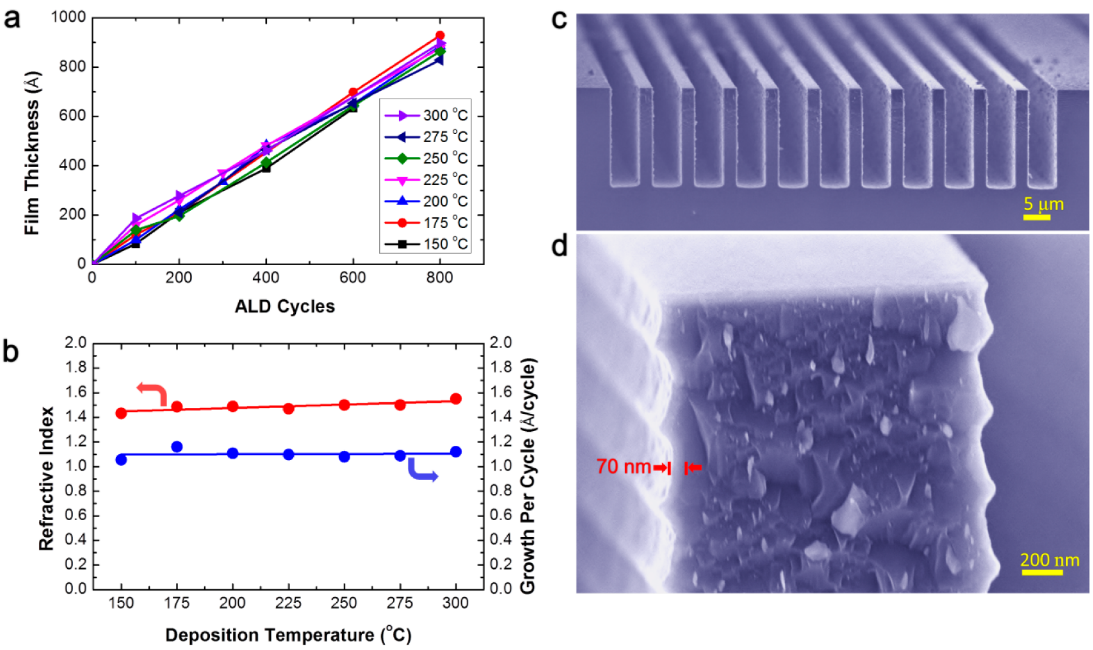

Figure 2. Growth characteristics of ALD Li_2S films. (a) Li_2S film thickness *versus* ALD cycles deposited at temperatures of 150–300 °C. (b) Refractive index and growth per cycle of ALD Li_2S films *versus* deposition temperature as measured by *ex situ* spectroscopic ellipsometry. (c,d) SEM images of ALD Li_2S film deposited in a high aspect ratio silicon trench substrate using 700 cycles at 150 °C: (c) lower magnification image showing a series of trenches and (d) higher magnification image showing the top of the trench.

In these equations, the symbol "|–" represents the surface, "g" denotes the gas phase, and a single LTB molecule reacts to form $LiS_{0.5}$ to simplify the analysis that follows. In eq 1a, LTB reacts with x thiol (–SH) groups (with x in the range of 0–1), liberating a fraction, x, of the –O^{t}Bu ligand into the gas phase as *tert*-butyl alcohol (HO^{t}Bu). In eq 1b, H_2S removes the remaining fraction, $(1 - x)$, of the –O^{t}Bu ligand to form stoichiometric $LiS_{0.5}$ and repopulate the surface with thiols. These equations assume that (1) thiol groups are the reactive species responsible for chemisorption of the LTB, (2) HO^{t}Bu is the only gas-phase product, and (3) the resulting film has the Li_2S stoichiometry. Assumptions 1 and 2 will be validated below, and the 2:1 stoichiometry will be confirmed in the characterization section.

With eqs 1a and 1b and the atomic masses, we can write the QCM mass ratio as

$$R = \Delta m/m_1 = 23/(80 - 73x) \qquad (2)$$

Based on the measured R values (see Figure SI-6a in the Supporting Information (SI)) and eq 2, we can extract the value for x *versus* the deposition temperature (Figure SI-6b in SI). At 150 °C, $x \sim 0.55$, indicating that approximately 55% of the –O^{t}Bu ligands are released into the gas phase during the LTB exposures. However, x decreases significantly with temperature to $x \sim 0.20$ at 300 °C. Evidently, the fraction of –O^{t}Bu ligands released during the LTB exposures is strongly dependent on the deposition temperature.

Figure 1c presents FTIR difference spectra after each LTB and H_2S exposure for the first, second, and 10th Li_2S ALD cycles. The first LTB exposure produces positive features in the ranges of 2865–2971 (antisymmetric and symmetric C–H stretching modes[31–33]), 1364–1471, and 912–999 cm^{-1} (both from CH_3 deformation and rocking modes[31,32]). The 1208 cm^{-1} feature is ascribed to C–O stretching from adsorbed –O^{t}Bu groups.[34] All of the aforementioned features are consistent with –O^{t}Bu ligands on the surface following the LTB exposure. Coincident with the appearance of the –O^{t}Bu features, a negative absorbance at 3739 cm^{-1} was observed during the first cycle (not shown), due to the removal of the ALD Al_2O_3 hydroxyl groups. In comparison, the first H_2S exposure generates negative absorbance features corresponding to the removal of CH_3 and C–O. It is noteworthy that the decreases from the first H_2S exposure are smaller than the corresponding increases from the first LTB exposure, suggesting that some of the –O^{t}Bu ligands remain on the Al_2O_3 surface. Beginning with the second cycle, however, the difference spectra following consecutive LTB and H_2S exposures become symmetric, indicating that the creation and removal of ligands are equivalent, as predicted by eqs 1a and 1b. A weak feature at ~2562 cm^{-1} from the S–H stretch[31,35] is seen to increase after the H_2S exposures and decrease following the LTB exposures, confirming the first assumption stated above (Figure 1c, inset).

Figure 1d shows the HO^{t}Bu intensity *versus* time recorded by QMS during the Li_2S ALD where each precursor was dosed twice in succession so that the second dose would reveal any possible background signals. (Note that HO^{t}Bu was the only product observed by QMS, validating assumption 2.) Figure 1d reveals that a majority of the HO^{t}Bu species are released during the H_2S exposures. The QMS measurements can be quantified using the QMS product ratio:

$$R' = A/B = x/(1-x) \qquad (3)$$

where A and B are the relative amounts of HO^{t}Bu released during the LTB and H_2S exposures, respectively. By integrating and averaging the QMS data in Figure 1d, we obtain $R' = 0.25$ so that $x = 0.20$. The value $x = 0.20$ derived from the QMS measurements compares favorably with the value $x = 0.22$ obtained by QCM at 225 °C, lending credence to both methods. In summary, the *in situ* QCM, FTIR, and QMS measurements all support the Li_2S growth mechanism proposed in eqs 1a and 1b. More details for the *in situ* studies are available in section 1 of SI.

Growth Characteristics, Film Morphology, Composition, and Structure of ALD Li_2S Nanofilms. Measurements using spectroscopic ellipsometry (SE) revealed that the nano-Li_2S growth was linear (see Figure 2a), yielding ~1.1 Å/cycle in the full range of 150−300 °C, as shown in Figure 2b. This value is ~10% higher than the value of 1.0 Å/cycle deduced from QCM, assuming a bulk Li_2S density of 1.66 g/cm^3.[36] The refractive index at 633 nm determined by SE is also nearly constant with temperature at ~1.4 (see Figure 2b). This value is substantially lower than the value of $n = 1.9$ reported for crystalline Li_2S.[37] The refractive index is an indirect measure of density and implies a lower density for the ALD Li_2S compared to crystalline Li_2S. By equating the QCM and SE growth per cycle values, we obtain a density of ~1.55 g/cm^3 for ALD Li_2S that is indeed lower than the bulk value. This lower density is consistent with the amorphous structure of ALD Li_2S determined by X-ray diffraction (XRD) measurements (see Figure SI-7 in SI). Annealing the Li_2S films at 500 °C for 2 h under Ar did not change the XRD patterns.

Using scanning electron microscopy (SEM), Figure 2c shows high aspect ratio micromachined Si trenches coated by 700 cycle ALD Li_2S at 150 °C and reveals uniform and conformal deposition along the structures. Figure 2d shows a higher magnification SEM image and emphasizes that the ALD Li_2S films are smooth and conformal such that the scalloped surface of the underlying Si is preserved. The Li_2S thickness extracted from Figure 2d is ~70 nm, in good agreement with the growth per cycle of 1.1 Å/cycle deduced from the SE measurements.

To investigate the composition of the ALD Li_2S films, we utilized X-ray photoelectron spectroscopy (XPS) and X-ray fluorescence spectroscopy (XRF). For the XPS, the Li_2S films were capped with ALD GaS_x/Al_2O_3 to protect against reaction with ambient air. A trilayered $Li_2S/GaS_x/Al_2O_3$ film was deposited at 200 °C and subjected to XPS depth profiling analysis (see

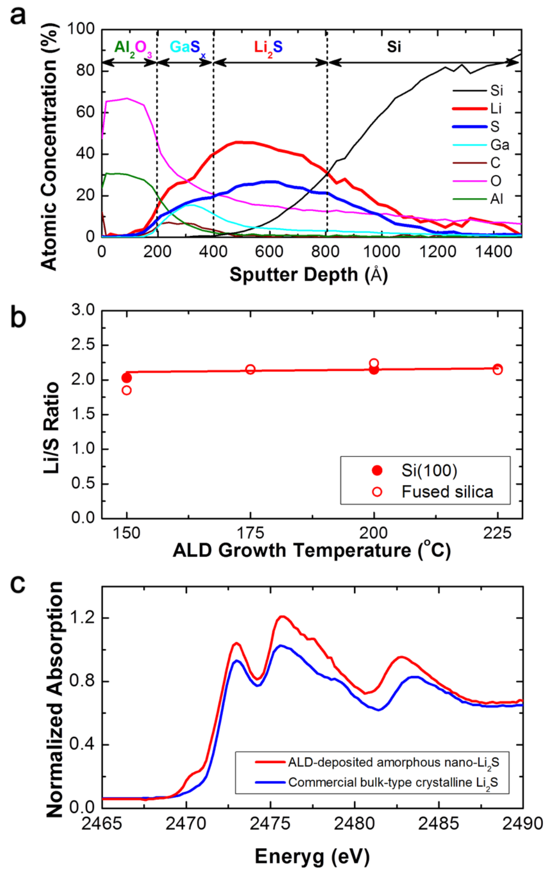

Figure 3. Chemical composition of ALD Li_2S films. (a) Atomic concentration *versus* depth for ALD $Li_2S/GaS_x/Al_2O_3$ trilayered film prepared using 600 ALD Li_2S cycles, 100 ALD GaS_x cycles, and 100 ALD Al_2O_3 cycles at 200 °C on a Si(100) substrate, measured by XPS depth profiling analysis. (b) X-ray fluorescence measurements of Li/S atomic ratio *versus* deposition temperature for ALD Li_2S films deposited on fused silica (open symbols) and Si(100) (closed symbols). Solid line is intended to guide the eye. (c) Normalized S K-edge XAS spectra for bulk-type crystalline Li_2S and ALD amorphous nano-Li_2S.

Figure 3a). The top Al_2O_3 capping layer consisted of Al and O, and the second GaS_x capping layer comprised Ga and S with some C, as expected,[38] but significant Al, O, and Li are also seen that may result from solid-state diffusion during the ALD or from intermixing during the XPS depth profiling. The ALD Li_2S is composed of Li and S with no C contamination, in agreement with the efficient and complete surface reactions observed by *in situ* FTIR. Figure 3a shows a ratio for Li/S of ~2.0, consistent with the expected Li_2S stoichiometry. The lack of carbon in the Li_2S and the 2:1 stoichiometry demonstrate that the trilayer is an effective capping strategy since reaction with the air would convert the Li_2S into Li_2O and then Li_2CO_3. As shown in Figure 3b, the Li/S ratio obtained from XRF remained nearly constant at ~2.0 over the full range of deposition temperatures and substrates.

Taken together, the elemental analysis of the ALD Li_2S films, combined with the *in situ* FTIR measurements, reveals that the ALD Li_2S films are pure and

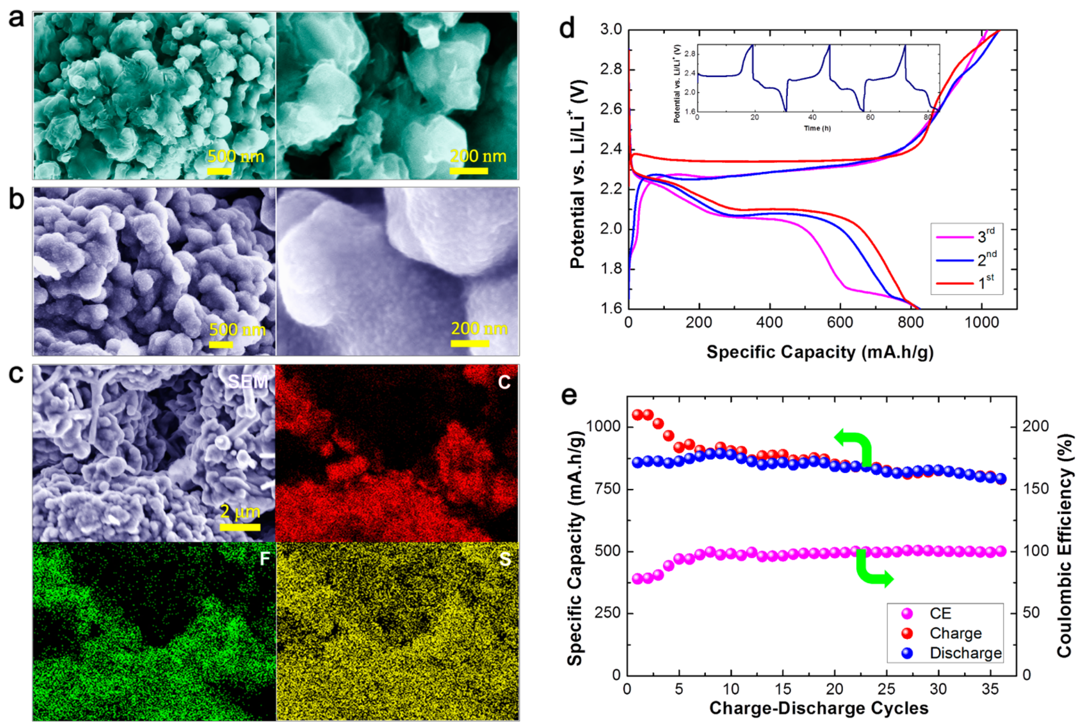

Figure 4. Electrochemical performance of ALD Li_2S. (a,b) SEM images of MCMB particles (a) before and (b) after 700 cycle ALD Li_2S coating. (c) EDX analysis of ALD Li_2S film deposited on MCMB particles, using 700 cycles at 200 °C: (top left) SEM image, (top right) C elemental map, (bottom left) F elemental map, and (bottom right) S elemental map. (d,e) Electrochemical characteristics of Li_2S films deposited on MCMB particles using 360 ALD Li_2S cycles at 300 °C: (d) charge−discharge profiles in the first three cycles (inset, first three cycles *versus* time), with a voltage window of 1.6−3.0 V and a current density of 55 mA/g, and (e) cyclability and Coulombic efficiency (CE) measured over 36 charge−discharge cycles.

stoichiometric. This was further substantiated using synchrotron X-ray absorption spectroscopy (XAS) measurements of ALD Li_2S films deposited on graphene nanosheets (GNS)[39] at 200 °C. Figure 3c compares the K-edge XAS spectra for ALD amorphous nano-Li_2S and bulk-type crystalline Li_2S. The ALD nano-Li_2S spectrum is very similar to that of the bulk-type crystalline Li_2S, with the exception of a small pre-edge feature at 2470.2 eV. This peak, which is lower than elemental sulfur's white line, has previously been associated with the terminal atom in polysulfides[40,41] and is likely related to surface termination of the ALD Li_2S thin film.

Electrochemical Performance of ALD Li_2S Nanofilms in Li−S Batteries. With the synthetic process for nano-Li_2S established, we investigated the electrochemical characteristics of the resulting materials and demonstrated the significance of precise control over the Li_2S size. Laminates (see Figure SI-11 in SI) were prepared using mesocarbon microbeans (MCMBs)[42] and subsequently coated with ALD Li_2S. After 700 Li_2S ALD cycles at 200 °C, the MCMB particles became more rounded and the laminate porosity was reduced (compare panels a and b in Figure 4). In addition, the ALD Li_2S film imparted a uniform texture to the surface comprising ~50 nm features. Elemental mapping using energy-dispersive X-ray spectroscopy (EDX) revealed uniform spatial distributions for C (MCMB), F (PVDF binder), and S (ALD Li_2S) (Figure 4c). Cross-sectional SEM demonstrated that the ALD Li_2S uniformly infiltrates the laminates (see Figure SI-12a−d in SI). Similar results were obtained from MCMB laminates coated with 360 cycle ALD Li_2S at 300 °C (see Figure SI-13 in SI).

Figure 4d shows charge−discharge profiles for the 360 cycle ALD Li_2S deposited on the MCMB laminates. A long, flat plateau is seen at ~2.34 V during the first charge, corresponding to the oxidative reaction: $8Li_2S \rightarrow S_8 + 16Li$. The first discharge shows a plateau at 2.2−2.3 V ($S_8 + 2Li \rightarrow Li_2S_8$), a slope at 2.1−2.2 V ($Li_2S_8 \rightarrow Li_2S_n$, $3 \leq n \leq 7$), a second plateau at 2.1 V ($Li_2S_n \rightarrow Li_2S_2$ or Li_2S), and a slope between 1.6 and 2.1 V ($Li_2S_2 \rightarrow Li_2S$). These observations are consistent with the electrochemical behavior of crystalline Li_2S,[7,17,43] but in our case, no potential barrier is seen for the first charge, as reported for microsized crystalline Li_2S by Yang et al.[9] Notably, the charge capacities are larger than the corresponding discharge capacities in the first three cycles, suggesting S shuttling as commonly observed during Li_2S oxidation.[7,44] Figure 4e shows the charge and discharge capacities recorded over 36 cycles and demonstrates a sustained capacity of ~800 mA·h/g corresponding to ~76% of the first charge capacity and 93% of the first discharge capacity. In addition, the ALD Li_2S films show a Coulombic efficiency of 100% beginning with the sixth cycle, implying that S shuttling was greatly alleviated. Two factors, based on previous studies, may contribute to the exceptional cyclability and sustained high capacity of ALD Li_2S nanofilms on MCMBs. First, the MCMB surface is rich in surface functional groups (*e.g.*, hydroxyl, carbonyl, and epoxy),[45,46] and recent studies[47,48] demonstrated that these same reactive surface groups on graphene oxide served to anchor polysulfides, thereby improving Li−S battery performance. The second factor relates to our use of a Cu current collector. A recent study[49] demonstrated that Cu nanoparticles could stabilize sulfur cathodes in Li−S batteries, and another work[50] showed that Cu foils were superior to Al foils for Cu_2S cathodes. Evidence for this second factor can be found in Figure 4d, where a new plateau emerges with the third discharge at ∼1.7 V, indicating Cu_xS formation. An early study[51] disclosed that Cu converted to Cu_xS in polysulfide-rich organic solutions.

We observed similar behavior for the MCMB electrodes coated with 700 cycle ALD Li_2S at 200 °C: a sustained capacity of ∼400 mA·h/g over 30 cycles and a high Coulombic efficiency of ∼100% starting from the seventh cycle (see Figure SI-14 in SI). The lower capacity compared to the 360 cycle ALD Li_2S film may stem from the greater film thickness which imposes a longer path for Li-ion and electron transport through the insulating Li_2S. No potential barrier was observed during the first charge for either of the ALD Li_2S films, and we attribute this to the amorphous and nanosized nature of our films which improves the Li-ion and electron transport. Also noteworthy is the excellent cyclability without the need for electrolyte additives such as $LiNO_3$ and polysulfides, which have been widely used in literature[9,17,43,44] (Figures 4e and SI-14).

To better understand the effects of using Cu current collectors, we deposited ALD Li_2S nanofilms on Cu foils and performed electrochemical testing. We investigated the long-term cyclability and rate capability of the ALD Li_2S films using 700 cycle ALD Li_2S deposited onto Cu foils at 200 °C. Figure 5a shows the first three charge−discharge profiles for this sample. The first charge profile shows the typical characteristics of Li_2S. However, the first discharge diverges somewhat from the expected Li_2S behavior. In particular, there is a slope between ∼2.6 and 2.4 V, a fast drop between 2.4 and 1.7 V, and a long declining plateau at ∼1.7 V. These changes can be ascribed to the Cu foil, for the oxidized S after the first charge can react with Cu to produce Cu_2S[52] and/or CuS.[53] Based on the characteristics of the three discharge profiles, the distinct plateau at 1.7 V suggests that Cu_2S is formed after the first charge. After the first discharge, both Cu and Li_2S would be produced. Thus, it is easy to understand that the following second charge exhibits the electrochemical characteristics of both Cu_xS (x = 1,2) and Li_2S, as illustrated in Figure 5a. As a consequence, the Cu foil affected the charge−discharge cycles of the ALD Li_2S, starting from

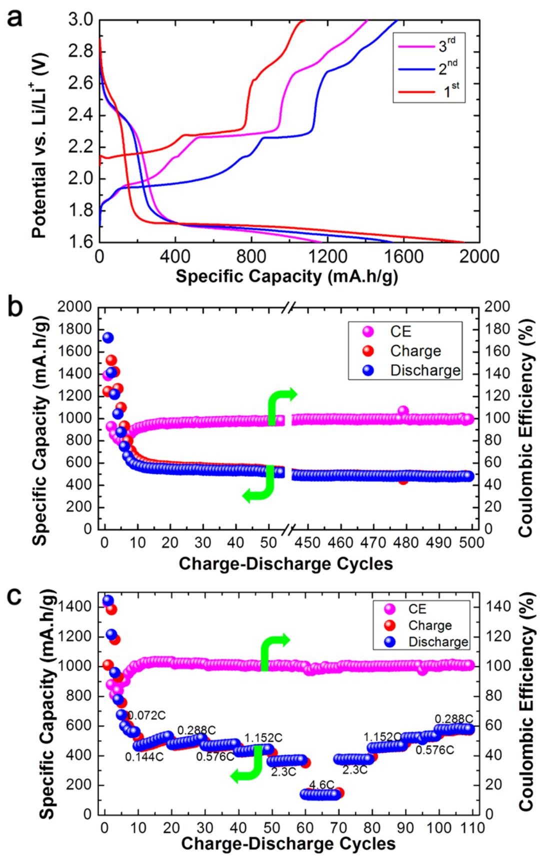

Figure 5. Electrochemical characteristics of Li_2S films deposited onto 2D planar Cu foils using 700 ALD Li_2S cycles at 200 °C. (a) Charge−discharge profiles in the first three cycles with a voltage window of 1.6−3.0 V and a current density of 840 mA/g. (b) Cyclability and Coulombic efficiency over 500 cycles. (c) Rate capability.

the first discharge. Similar effects of Cu foils have been reported with S[49] and other metal sulfides.[50,54] In comparison to the discharge plateau of ∼1.7, Zheng *et al.*[49] reported a much lower discharge plateau of 1.0−1.3 V using Cu nanoparticles as S stabilizers. We note that, due to the involvement of Cu, there is extra capacity observed in the first three cycles (except for the first charge). This 700 cycle ALD Li_2S thin film on Cu foil demonstrates very good cycling performance at a current density of 840 mA/g, as shown in Figure 5b. Except for the capacity drop in the first 10 cycles (probably due to partial dissolution of Li_2S), the ALD Li_2S film remained nearly constant at ∼500 mA·h/g over 500 cycles and achieved a Coulombic efficiency of ∼100% from the 15th cycle. Furthermore, the 700 cycle ALD Li_2S thin film on Cu foil also exhibits very good rate capabilities, as shown in Figure 5c, except for fast capacity fading in the first five cycles. This ALD Li_2S film maintained stable capacities of 510, 500, 480, and 380 mA·h/g at current densities of 168 (0.144C), 336 (0.288C), 672 (0.576C), 1344 (1.152 C), and 2688 mA/g (2.3C), respectively. At the very high current density of 5376 mA/g (4.6C), the ALD Li_2S film exhibited a capacity of ∼135 mA·h/g. The exceptional performance of ALD

Li_2S might derive from the Cu current collector, as discussed above. In addition, the thin ALD Li_2S layers probably have facilitated the formation of Cu_xS as the actual active material.

As shown above, our ALD process yields precisely controlled nanoscale Li_2S films on 2D Cu foils and 3D layers of MCMBs. The results demonstrated that ALD Li_2S is viable for developing high-performance and high-energy Li−S microbatteries. Given the conformal nature of ALD, it should also be feasible to synthesize nanophase composites with high Li_2S loadings for bulk-type Li−S batteries, using ALD on high-surface-area supports. Indeed, our preliminary studies using high-surface-area GNS have produced Li_2S loadings as high as 67 wt %, and the resulting composites exhibit excellent cycling performance in Li−S batteries. This work is ongoing and will be described in future publications.

CONCLUSIONS

In summary, we introduced a new vapor-phase method for synthesizing amorphous nano-Li_2S that provides atomic-level thickness control at low temperatures. The exceptionally uniform and conformal nanoscale films enabled Li_2S to achieve high performance as a Li−S cathode. No potential barrier for activation was seen during charging, and the ALD Li_2S exhibited a high, sustained capacity of up to 800 mA·h/g, excellent cyclability, and high Coulombic efficiency without the need for electrolyte additives. Besides the amorphous structure and precise nanoscale thickness afforded by the ALD Li_2S films, the excellent electrochemical performance also stems from using the Cu current collector and MCMBs. This atomic-controllable vapor-phase synthesis route and the resulting nanoscale conformal Li_2S films are significant for developing high-energy Li−S batteries.

EXPERIMENTAL SECTION

Vapor-Phase Li_2S ALD. These experiments utilized a custom viscous flow, hot-walled ALD reactor[55] composed of a stainless steel flow tube with a length of 100 cm and an inner diameter of 5 cm. The Li_2S ALD was performed by alternately dosing lithium *tert*-butoxide ($LiOC(CH_3)_3$) or LiO^tBu (98%, Strem Chemicals, Inc., USA) and hydrogen sulfide (H_2S, 1% in N_2, Matheson Tri-gas, USA) with N_2 purging periods between each dose. To provide sufficient vapor pressure, the solid LTB was heated to 140 °C in a stainless steel reservoir, and 50 sccm ultrahigh purity N_2 (UHP, 99.999%) was diverted through the reservoir during the LTB exposures. This yielded a partial pressure of ~0.01 Torr LTB in the flow tube. The 1% H_2S was stored in a pressure-regulated lecture bottle. A series of needle valves were used to deliver 1% H_2S pressure pulses of ~0.2 Torr during the H_2S exposures. Li_2S is air-sensitive and reacts readily with oxygen and moisture to form lithium sulfate and lithium hydroxide. The latter subsequently forms lithium carbonate by reaction with CO_2. Consequently, an Ar-filled glovebag was installed at the end of the ALD reactor flow tube to provide inert conditions for loading and unloading the coated substrates.

***In Situ* Measurements during Li_2S ALD.** The Li_2S ALD was systematically investigated using an *in situ* quartz crystal microbalance. The QCM studies were conducted using a modified Maxtek model BSH-150 sensor head with an RC quartz crystal sensor (CNT06RCIA, Colnatec). The crystals were sealed within the sensor head using a high-temperature conducting epoxy (P1011, Epotek), and the sensor head was modified to provide back-side purging of the crystal to confine growth to the front surface.[55,56] During the ALD, a constant 300 sccm flow of UHP N_2 passed through the flow tube at a pressure of ~1.2 Torr. The Li_2S ALD timing can be described as $t_1-t_2-t_3-t_4$, with t_1 and t_3 being the dosing times for the LTB and H_2S, respectively, and t_2 and t_4 being the corresponding purge times, with all times in seconds (s). Optimal timing for the saturated Li_2S growth was determined by QCM measurements. Prior to the Li_2S ALD, an ALD Al_2O_3 film was deposited on the QCM surface using alternating trimethylaluminum (TMA) and H_2O exposures with the timing sequence 1−5−1−5 s to establish a uniform starting surface.

Additional *in situ* studies were performed using quadrupole mass spectrometry and Fourier transform infrared spectroscopy to explore the surface chemical reactions responsible for the Li_2S ALD. The QMS (Stanford Research Systems, model RGA300) was located downstream from the sample position in a differentially pumped, high-vacuum chamber separated from the reactor by a 35 μm orifice. *In situ* QMS measurements were performed at 225 °C to detect and quantify the gas-phase products of the Li_2S ALD. First, a comprehensive survey was conducted of all masses between m/z = 2−100 to identify the products of the LTB and H_2S half reactions. The only product observed was *tert*-butyl alcohol, as evidenced by peaks at m/e = 59, 41, and 31 in the expected ratios from the NIST database.[57]

The FTIR (Nicolet 6700 FTIR spectrometer, Thermo Scientific) was operated in transmission mode in a separate ALD reactor as described previously.[30] The FTIR beam passed through the reactor *via* IR-transparent KBr windows. Pneumatically actuated gate valves were closed during the precursor exposures to prevent growth on the KBr windows. Substrates for FTIR measurements were prepared by pressing ZrO_2 nanopowder (Aldrich, particle size <100 nm, specific surface area >25 m^2/g) into a stainless steel grid.[58,59] The grids were fabricated by photochemical machining (Fotofab, Inc.) to be 50 μm thick with 50 μm bars and 200 μm square openings. ZrO_2 is relatively transparent between 4000 and 800 cm^{-1}, the frequency range of interest for identifying surface functional groups, and the high surface area amplified the IR absorption features. The nanopowder-filled grid was mounted onto a temperature-regulated stage. This stage was then loaded into the FTIR reactor so that the IR beam passed through the center of the grid. During the *in situ* FTIR measurements, the substrate temperature was maintained at 225 °C by the heated stage, and the reactor walls were also heated to ~225 °C to prevent precursor condensation. The FTIR substrates were first passivated with ALD Al_2O_3 by performing eight TMA/H_2O cycles. Next, 10 alternating exposures to LTB and 100% H_2S were performed with the optimized timing sequence, and FTIR spectra were recorded after each precursor exposure.

Characterization of ALD Li_2S Films. The ALD Li_2S films were deposited onto Si(100), fused silica, micromachined Si trench wafers, copper foils, and graphite particles and subsequently characterized using a variety of techniques. To preserve the air-sensitive Li_2S coatings during transport to the characterization tools, the Li_2S-coated substrates were loaded into hermetically sealed containers inside of the Ar-filled glovebag. Spectroscopic ellipsometry (alpha-SE, J.A. Woollam Co.) was employed, and the ellipsometric data were fit using a Cauchy model to extract the film thickness and refractive index. The SE measurements were conducted on ALD nano-Li_2S films deposited on Si(100) substrates with the native oxide intact prepared in the temperature range of 150−300 °C. These measurements were performed inside of an Ar-filled glovebag. The film morphology was examined by FE-SEM (Hitachi S4700) equipped with EDX. Due to the air-sensitive nature of Li_2S, the ALD nano-Li_2S samples were protected by transporting them in Ar-filled containers. Although the ALD nano-Li_2S films received a brief exposure (∼10 s) to air when loading into the SEM, we believe this had a negligible effect on the morphology as explained in the Supporting Information. The Li_2S films were annealed in a muffle furnace (type 1300, Thermo Scientific) located in an Ar-filled glovebox with moisture and oxygen levels below 1 ppm.

The crystallinity of the as-deposited and annealed Li_2S films was determined by X-ray diffraction (D8 Advance, Bruker). For these measurements, the samples were covered by a Kapton film that had previously been coated with ∼20 nm ALD Al_2O_3 to protect them from moisture. Both Kapton and Al_2O_3 are X-ray transparent, and we have previously demonstrated that this covering provides excellent protection from the air.[38,60] The film composition was measured by X-ray fluorescence spectroscopy (ED 2000, Oxford Instruments) and X-ray photoelectron spectroscopy (PHI Quantum 2000). Before the XRF measurements, the Li_2S films were covered by ALD Al_2O_3-coated Kapton films, as used for the XRD measurements. The XPS measurements were conducted by Evans Analytical Group (Sunnyvale, CA). The XPS was equipped with a monochromated Al Kα (1486.6 eV) X-ray source and an airless entry system. Depth profiling measurements were performed using Ar^+ sputtering. The sputter rate was calibrated using SiO_2, accounting for a SiO_2-equivalent rate of 7.81 Å/min. The analysis area was 1400 × 300 μm.

X-ray absorption was performed at the Advanced Photon Source, sector 13-ID-E in fluorescence mode. The ALD sample consisted of Li_2S grown on graphene nanosheets, and the bulk standard was purchased from Sigma-Aldrich. Samples were spread on sulfur-free tape (Premier Lab Supply) and sealed in aluminized Kapton. Each spectrum showed little evolution over repeated scans and was not corrected for self-absorption.

Electrochemical Testing of ALD Li_2S Films and Nanocomposites. To evaluate the electrochemical properties of the ALD Li_2S, nanofilms were deposited in the temperature range of 150−300 °C onto Cu foils and graphite laminates made from mesocarbon microbeans (MCMB-1028, a type of graphite powder) and subsequently tested as a LIB electrode material. The graphite laminates were made by casting a slurry of 90 wt % MCMB, 2 wt % vapor-grown carbon fiber, and 8 wt % poly(vinylidene fluoride) (PVDF, Kureha 1100) binder dispersed in *N*-methyl-2-pyrrolidone onto copper foils, as detailed previously.[42] The MCMB particles had a surface area of 1.96 m^2/g, and the dried laminates were 56 μm thick with a porosity of 42.2%. The Li_2S-coated substrates were assembled into CR2032 coin cells in an Ar-filled glovebox. Li metal was used as the counter/reference electrode, and a Celgard 2400 membrane was used as the separator. The electrolyte used was 1 M lithium bis(trifluoromethanesulfonyl)imide (Sigma-Aldrich) in 1,3-dioxolane (DOL, Sigma-Aldrich) and 1,2-dimethoxyethane (DME, Sigma-Aldrich) (DOL/DME = 1:1 by volume). Charge/discharge testing was performed on an Arbin 2043 electrochemical tester using a voltage window of 1.6−3.0 V for the Li_2S electrodes.

Conflict of Interest: The authors declare no competing financial interest.

Acknowledgment. This work was supported as part of the Center for Electrical Energy Storage: Tailored Interfaces, an Energy Frontier Research Center funded by the U.S. Department of Energy, Office of Science, Office of Basic Energy Sciences. Electron microscopy was performed at the Electron Microscopy Center for Materials Research (EMCMR) at Argonne National Laboratory. Use of the EMCMR was supported by the U.S. Department of Energy, Office of Science, Office of Basic Energy Sciences, under Contract No. DE-AC02-06CH11357 operated by UChicago Argonne, LLC. XAS was performed at GeoSoilEnviroCARS (Sector 13), Advanced Photon Source (APS), Argonne National Laboratory. GeoSoilEnviroCARS is supported by the National Science Foundation-Earth Sciences (EAR-1128799) and Department of Energy-GeoSciences (DE-FG02-94ER14466). Use of the Advanced Photon Source was supported by the U.S. Department of Energy, Office of Science, Office of Basic Energy Sciences, under Contract No. DE-AC02-06CH11357. We greatly appreciate Dr. Paul A. Fenter, a Scientist in Chemical Sciences and Engineering Division at Argonne National Laboratory, for his valuable discussions and review of the paper, and the generous use of his experimental facilities. X.M. appreciates the financial support from a Canada NSERC Postdoctoral Fellowship.

Supporting Information Available: Further details on *in situ* studies of Li_2S ALD (Figures SI-1 to SI-6), characterization of ALD Li_2S films (Figures SI-7 to SI-10), and electrochemical performance of ALD Li_2S films (Figures SI-11 to SI-15). This material is available free of charge *via* the Internet at http://pubs.acs.org.

REFERENCES AND NOTES

1. Yang, Z. G.; Zhang, J. L.; Kintner-Meyer, M. C. W.; Lu, X. C.; Choi, D. W.; Lemmon, J. P.; Liu, J. Electrochemical Energy Storage for Green Grid. *Chem. Rev.* **2011**, *111*, 3577–3613.
2. Thackeray, M. M.; Wolverton, C.; Isaacs, E. D. Electrical Energy Storage for Transportation: Approaching the Limits of, and Going beyond, Lithium-Ion Batteries. *Energy Environ. Sci.* **2012**, *5*, 7854–7863.
3. Liu, J.; Zhang, J. G.; Yang, Z. G.; Lemmon, J. P.; Imhoff, C.; Graff, G. L.; Li, L. Y.; Hu, J. Z.; Wang, C. M.; Xiao, J.; *et al.* Materials Science and Materials Chemistry for Large Scale Electrochemical Energy Storage: From Transportation to Electrical Grid. *Adv. Funct. Mater.* **2013**, *23*, 929–946.
4. Bruce, P. G.; Freunberger, S. A.; Hardwick, L. J.; Tarascon, J. M. Li-O_2 and Li-S Batteries with High Energy Storage. *Nat. Mater.* **2012**, *11*, 19–29.
5. Manthiram, A.; Fu, Y. Z.; Su, Y. S. Challenges and Prospects of Lithium-Sulfur Batteries. *Acc. Chem. Res.* **2013**, *46*, 1125–1134.
6. Evers, S.; Nazar, L. F. New Approaches for High Energy Density Lithium-Sulfur Battery Cathodes. *Acc. Chem. Res.* **2013**, *46*, 1135–1143.
7. Zhang, S. S. Liquid Electrolyte Lithium/Sulfur Battery: Fundamental Chemistry, Problems, and Solutions. *J. Power Sources* **2013**, *231*, 153–162.
8. Zhang, S. S. New Insight into Liquid Electrolyte of Rechargeable Lithium/Sulfur Battery. *Electrochim. Acta* **2013**, *97*, 226–230.
9. Yang, Y.; Zheng, G. Y.; Misra, S.; Nelson, J.; Toney, M. F.; Gui, Y. High-Capacity Micrometer-Sized Li_2S Particles as Cathode Materials for Advanced Rechargeable Lithium-Ion Batteries. *J. Am. Chem. Soc.* **2012**, *134*, 15387–15394.
10. Cai, K. P.; Song, M. K.; Cairns, E. J.; Zhang, Y. G. Nanostructured Li_2S-C Composites as Cathode Material for High-Energy Lithium/Sulfur Batteries. *Nano Lett.* **2012**, *12*, 6474–6479.
11. Jeong, S.; Bresser, D.; Buchholz, D.; Winter, M.; Passerini, S. Carbon Coated Lithium Sulfide Particles for Lithium Battery Cathodes. *J. Power Sources* **2013**, *235*, 220–225.
12. Hassoun, J.; Sun, Y. K.; Scrosati, B. Rechargeable Lithium Sulfide Electrode for a Polymer Tin/Sulfur Lithium-Ion Battery. *J. Power Sources* **2011**, *196*, 343–348.
13. Takeuchi, T.; Kageyama, H.; Nakanishi, K.; Tabuchi, M.; Sakaebe, H.; Ohta, T.; Senoh, H.; Sakai, T.; Tatsumi, K. All-Solid-State Lithium Secondary Battery with Li_2S-C Composite Positive Electrode Prepared by Spark-Plasma-Sintering Process. *J. Electrochem. Soc.* **2010**, *157*, A1196–A1201.
14. Nagao, M.; Hayashi, A.; Tatsumisago, M. High-Capacity Li_2S-Nanocarbon Composite Electrode for All-Solid-State Rechargeable Lithium Batteries. *J. Mater. Chem.* **2012**, *22*, 10015–10020.
15. Hayashi, A.; Ohtsubo, R.; Tatsumisago, M. Electrochemical Performance of All-Solid-State Lithium Batteries with Mechanochemically Activated Li_2S-Cu Composite Electrodes. *Solid State Ionics* **2008**, *179*, 1702–1705.
16. Hayashi, A.; Ohtsubo, R.; Ohtomo, T.; Mizuno, F.; Tatsumisago, M. All-Solid-State Rechargeable Lithium Batteries with Li_2S as a Positive Electrode Material. *J. Power Sources* **2008**, *183*, 422–426.
17. Yang, Z. C.; Guo, J. C.; Das, S. K.; Yu, Y. C.; Zhou, Z. H.; Abruna, H. D.; Archer, L. A. *In Situ* Synthesis of Lithium

Sulfide-Carbon Composites as Cathode Materials for Rechargeable Lithium Batteries. *J. Mater. Chem. A* **2013**, *1*, 1433–1440.

18. Zhou, Y. N.; Wu, C. L.; Zhang, H.; Wu, X. J.; Fu, Z. W. Electrochemical Reactivity of Co-Li_2S Nanocomposite for Lithium-Ion Batteries. *Electrochim. Acta* **2007**, *52*, 3130–3136.
19. Wu, F. X.; Magasinski, A.; Yushin, G. Nanoporous Li_2S and MWCNT-Linked Li_2S Powder Cathodes for Lithium-Sulfur and Lithium-Ion Battery Chemistries. *J. Mater. Chem. A* **2014**, *2*, 6064–6070.
20. Yang, Y.; McDowell, M. T.; Jackson, A.; Cha, J. J.; Hong, S. S.; Cui, Y. New Nanostructured Li_2S/Silicon Rechargeable Battery with High Specific Energy. *Nano Lett.* **2010**, *10*, 1486–1491.
21. Lin, Z.; Liu, Z. C.; Dudney, N. J.; Liang, C. D. Lithium Superionic Sulfide Cathode for All-Solid Lithium-Sulfur Batteries. *ACS Nano* **2013**, *7*, 2829–2833.
22. Yang, Y.; Zheng, G. Y.; Cui, Y. Nanostructured Sulfur Cathodes. *Chem. Soc. Rev.* **2013**, *42*, 3018–3032.
23. Hayashi, A.; Tatsumisago, M. Recent Development of Bulk-Type Solid-State Rechargeable Lithium Batteries with Sulfide Glass-Ceramic Electrolytes. *Electron. Mater. Lett.* **2012**, *8*, 199–207.
24. Tatsumisago, M.; Nagao, M.; Hayashi, A. Recent Development of Sulfide Solid Electrolytes and Interfacial Modification for All-Solid-State Rechargeable Lithium Batteries. *J. Asian Ceram. Soc.* **2013**, *1*, 17–25.
25. Agrawal, R. C.; Gupta, R. K. Superionic Solids: Composite Electrolyte Phase: An Overview. *J. Mater. Sci.* **1999**, *34*, 1131–1162.
26. Kamaya, N.; Homma, K.; Yamakawa, Y.; Hirayama, M.; Kanno, R.; Yonemura, M.; Kamiyama, T.; Kato, Y.; Hama, S.; Kawamoto, K.; *et al.* A Lithium Superionic Conductor. *Nat. Mater.* **2011**, *10*, 682–686.
27. George, S. M. Atomic Layer Deposition: An Overview. *Chem. Rev.* **2010**, *110*, 111–131.
28. Meng, X.; Yang, X. Q.; Sun, X. Emerging Applications of Atomic Layer Deposition for Lithium-Ion Battery Studies. *Adv. Mater.* **2012**, *24*, 3589–615.
29. Marichy, C.; Bechelany, M.; Pinna, N. Atomic Layer Deposition of Nanostructured Materials for Energy and Environmental Applications. *Adv. Mater.* **2012**, *24*, 1017–1032.
30. Elam, J. W.; Libera, J. A.; Hryn, J. N. Indium Oxide ALD Using Cyclopentadienyl Indium and Mixtures of H_2O and O_2. *ECS Trans.* **2011**, *41*, 147–155.
31. Coates, J. *Encyclopedia of Analytical Chemistry*; John Wiley & Sons Ltd.: Chichester, UK, 2000; pp 10815−10837.
32. Burton, B. B.; Kang, S. W.; Rhee, S. W.; George, S. M. SiO_2 Atomic Layer Deposition Using Tris(dimethylamino)silane and Hydrogen Peroxide Studied by *In Situ* Transmission FTIR Spectroscopy. *J. Phys. Chem. C* **2009**, *113*, 8249–8257.
33. Cameron, M. A.; George, S. M. ZrO_2 Film Growth by Chemical Vapor Deposition Using Zirconium Tetra-*tert*-butoxide. *Thin Solid Films* **1999**, *348*, 90–98.
34. Cavanagh, A. S.; Lee, Y.; Yoon, B.; George, S. M. Atomic Layer Deposition of LiOH and Li_2CO_3 Using Lithium *t*-Butoxide as the Lithium Source. *ECS Trans.* **2010**, *33*, 223–229.
35. Miller, B. J.; Howard, D. L.; Lane, J. R.; Kjaergaard, H. G.; Dunn, M. E.; Vaida, V. SH-Stretching Vibrational Spectra of Ethanethiol and *tert*-Butylthiol. *J. Phys. Chem. A* **2009**, *113*, 7576–7583.
36. Zheng, J. M.; Gu, M.; Wang, C. M.; Zuo, P. J.; Koech, P. K.; Zhang, J. G.; Liu, J.; Xiao, J. Controlled Nucleation and Growth Process of Li_2S_2/Li_2S in Lithium-Sulfur Batteries. *J. Electrochem. Soc.* **2013**, *160*, A1992–A1996.
37. Bertheville, B.; Bill, H.; Hagemann, H. Experimental Raman Scattering Investigation of Phonon Anharmonicity Effects in Li_2S. *J. Phys.: Condens. Matter* **1998**, *10*, 2155.
38. Meng, X.; Libera, J. A.; Fister, T. T.; Zhou, H.; Hedlund, J. K.; Fenter, P.; Elam, J. W. Atomic Layer Deposition of Gallium Sulfide Films Using Hexakis(dimethylamido)digallium and Hydrogen Sulfide. *Chem. Mater.* **2014**, *26*, 1029–1039.
39. Meng, X. B.; Geng, D. S.; Liu, J. A.; Li, R. Y.; Sun, X. L. Controllable Synthesis of Graphene-Based Titanium Dioxide Nanocomposites by Atomic Layer Deposition. *Nanotechnology* **2011**, *22*, 165602.
40. Pascal, T. A.; Wujcik, K. H.; Velasco-Velez, J.; Wu, C.; Teran, A. A.; Kapilashrami, M.; Cabana, J.; Guo, J.; Salmeron, M.; Balsara, N.; *et al.* X-ray Absorption Spectra of Dissolved Polysulfides in Lithium−Sulfur Batteries from First-Principles. *J. Phys. Chem. Lett.* **2014**, *5*, 1547–1551.
41. Patel, M. U. M.; Arcon, I.; Aquilanti, G.; Stievano, L.; Mali, G.; Dominko, R. X-ray Absorption Near-Edge Structure and Nuclear Magnetic Resonance Study of the Lithium−Sulfur Battery and its Components. *ChemPhysChem* **2014**, *15*, 894–904.
42. Qin, Y.; Chen, Z. H.; Lu, W. Q.; Amine, K. Electrolyte Additive To Improve Performance of MCMB/$LiNi_{1/3}Co_{1/3}Mn_{1/3}O_2$ Li-Ion Cell. *J. Power Sources* **2010**, *195*, 6888–6892.
43. Han, K.; Shen, J.; Hayner, C. M.; Ye, H.; Kung, M. C.; Kung, H. H. Li_2S-Reduced Graphene Oxide Nanocomposites as Cathode Material for Lithium Sulfur Batteries. *J. Power Sources* **2014**, *251*, 331–337.
44. Diao, Y.; Xie, K.; Xiong, S. Z.; Hong, X. B. Shuttle Phenomenon: The Irreversible Oxidation Mechanism of Sulfur Active Material in Li-S Battery. *J. Power Sources* **2013**, *235*, 181–186.
45. Alcántara, R.; Fernández Madrigal, F. J.; Lavela, P.; Tirado, J. L.; Jiménez Mateos, J. M.; Gómez de Salazar, C.; Stoyanova, R.; Zhecheva, E. Characterisation of Mesocarbon Microbeads (MCMB) as Active Electrode Material in Lithium and Sodium Cells. *Carbon* **2000**, *38*, 1031–1041.
46. Wang, Y.-G.; Chang, Y.-C.; Ishida, S.; Korai, Y.; Mochida, I. Stabilization and Carbonization Properties of Mesocarbon Microbeads (MCMB) Prepared from a Synthetic Naphthalene Isotropic Pitch. *Carbon* **1999**, *37*, 969–976.
47. Ji, L.; Rao, M.; Zheng, H.; Zhang, L.; Li, Y.; Duan, W.; Guo, J.; Cairns, E. J.; Zhang, Y. Graphene Oxide as a Sulfur Immobilizer in High Performance Lithium/Sulfur Cells. *J. Am. Chem. Soc.* **2011**, *133*, 18522–18525.
48. Wang, H. L.; Yang, Y.; Liang, Y. Y.; Robinson, J. T.; Li, Y. G.; Jackson, A.; Cui, Y.; Dai, H. J. Graphene-Wrapped Sulfur Particles as a Rechargeable Lithium-Sulfur Battery Cathode Material with High Capacity and Cycling Stability. *Nano Lett.* **2011**, *11*, 2644–2647.
49. Zheng, S.; Yi, F.; Li, Z.; Zhu, Y.; Xu, Y.; Luo, C.; Yang, J.; Wang, C. Copper-Stabilized Sulfur-Microporous Carbon Cathodes for Li−S Batteries. *Adv. Funct. Mater.* **2014**, *24*, 4156–4163.
50. Jache, B.; Mogwitz, B.; Klein, F.; Adelhelm, P. Copper Sulfides for Rechargeable Lithium Batteries: Linking Cycling Stability to Electrolyte Composition. *J. Power Sources* **2014**, *247*, 703–711.
51. Eichinger, G.; Fritz, H. P. Copper Based Electrodes in Organic Electrolyte Solutions—III. The Discharge Mechanism of Copper(II) Sulphide in Some Organic Solvents. *Electrochim. Acta* **1975**, *20*, 753–757.
52. Ni, S. B.; Li, T.; Yang, X. L. Fabrication of Cu_2S on Cu Film Electrode and Its Application in Lithium Ion Battery. *Thin Solid Films* **2012**, *520*, 6705–6708.
53. Wang, Y. R.; Zhang, X. W.; Chen, P.; Liao, H. T.; Cheng, S. Q. *In Situ* Preparation of CuS Cathode with Unique Stability and High Rate Performance for Lithium Ion Batteries. *Electrochim. Acta* **2012**, *80*, 264–268.
54. Wang, Y. R.; Liao, H. T.; Wang, J.; Qian, X. F.; Zhu, Y. C.; Cheng, S. Q. Effects of Current Collectors on Electrochemical Performance of FeS_2 for Li-Ion Battery. *Int. J. Electrochem. Sci.* **2013**, *8*, 4002–4009.
55. Elam, J. W.; Groner, M. D.; George, S. M. Viscous Flow Reactor with Quartz Crystal Microbalance for Thin Film Growth by Atomic Layer Deposition. *Rev. Sci. Instrum.* **2002**, *73*, 2981–2987.
56. Elam, J. W.; Pellin, M. J. $GaPO_4$ Sensors for Gravimetric Monitoring during Atomic Layer Deposition at High Temperatures. *Anal. Chem.* **2005**, *77*, 3531–3535.
57. Linstrom, P. J.; Mallard, W. G. *NIST Chemistry WebBook*, NIST Standard Reference Database Number 69; National Institute of Standards and Technology: Gaithersburg, MD, http://webbook.nist.gov (accessed January 17, **2014**).

58. Ferguson, J. D.; Weimer, A. W.; George, S. M. Atomic Layer Deposition of Ultrathin and Conformal Al_2O_3 Films on BN Particles. *Thin Solid Films* **2000**, *371*, 95–104.
59. Ballinger, T. H.; Wong, J. C. S.; Yates, J. T. Transmission Infrared-Spectroscopy of High Area Solid-Surfaces: A Useful Method for Sample Preparation. *Langmuir* **1992**, *8*, 1676–1678.
60. Meng, X.; He, K.; Su, D.; Zhang, X.; Sun, C.; Ren, Y.; Wang, H.-H.; Weng, W.; Trahey, L.; Canlas, C. P.; *et al.* Gallium Sulfide−Single-Walled Carbon Nanotube Composites: High-Performance Anodes for Lithium-Ion Batteries. *Adv. Funct. Mater.* **2014**, *24*, 5435–5442.